



Bond Behavior in Flexural Members: Numerical Studies

Ankit Bhardwaj¹ · Vasant Matsagar² · A. K. Nagpal² · Sandeep Chaudhary³

Received: 9 May 2020 / Accepted: 16 October 2020 / Published online: 28 October 2020
© Korean Society of Steel Construction 2020

Abstract

Adhesive bonding has recently emerged as an alternative to shear stud connection in steel–concrete composite flexural members. Research on adhesive-bonded steel–concrete composite flexural members is in a preliminary stage, and the behavior of the bond layer in these structures is not well understood yet. A three-dimensional finite element model is developed and used to conduct the parametric investigations. The developed model is validated with experimental results available in the literature. The behavior of the bond layer is defined in terms of normal stress, normal strain, shear stress, and shear strain. Seven different parameters are studied regarding their effect on the behavior of the bond layer. The parameters include load proportion factor, longitudinal distribution of load, transverse distribution of load, width of concrete slab, depth of the concrete slab, Young's modulus of the adhesive and transverse location of the adhesive fiber. Parametric investigations are carried out to establish the relevance of parameters in terms of their effect on the behavior of the bond layer. The most significant parameters are identified as load proportion factor, longitudinal distribution of load, and Young's modulus of adhesive.

Keywords Composite beams · Bonded · Bond layer · Shear connection · Finite element analysis · Young's modulus

1 Introduction

The connection between steel and concrete plays an important role in determining the stiffness and strength of steel–concrete composite members. Such connection, referred to as shear connection, resists horizontal slip and vertical separation of steel and concrete components, and enables the steel and concrete components of the composite members to behave as a unit. Shear studs are most

popularly used for shear connection. However, shear studs cause stress concentration in the concrete and may exhibit significant slip, which results in partial interaction (Oehlers and Bradford 1995). Moreover, such construction often leads to shrinkage cracks in concrete (Lebet and Ducret 1998), as it mainly involves the in-situ casting of concrete.

Composite structures have been investigated for several aspects, such as service load behavior (Chaudhary et al. 2008; Pendharkar et al. 2011, 2015; Ramnavas et al. 2015), behavior of continuous composite structures (Gupta et al. 2015; Tadesse et al. 2012; Varshney et al. 2019), and behavior of composite beams in frames (Pendharkar et al. 2017; Ramnavas et al. 2017a, b; Varshney et al. 2013). Effective width (Amadio et al. 2004; Nie et al. 2008; Wang and Nie 2015), effect of reinforcement detailing (Kumar and Chaudhary 2019), coupled beams (Zheng et al. 2014), perfect connection (Souici et al. 2015) and imperfect connection (Gara et al. 2010) also have been studied for composite structures. Behavior of composite structures under seismic load has also been examined (Naghavi et al. 2019; Rahnavard et al. 2016, 2017, 2018). Several innovative connections between steel and concrete to achieve better performance of composite structures have been investigated, which include angle connector (Balasubramanian and Rajaram 2016), hat shaped connector (Kim et al. 2011), I-shape connector (Mazoz et al.

✉ Sandeep Chaudhary
schaudhary@iiti.ac.in

Ankit Bhardwaj
ank.bhardwaj@gmail.com

Vasant Matsagar
matsagar@civil.iitd.ac.in

A. K. Nagpal
aknagpal_iitd@yahoo.co.in

¹ Department of Civil Engineering, Government Engineering College Bharatpur, Bharatpur 321303, India

² Department of Civil Engineering, Indian Institute of Technology (IIT) Delhi, Hauz Khas, New Delhi 110016, India

³ Department of Civil Engineering, Indian Institute of Technology (IIT) Indore, Simrol, Indore 453552, India

composite structures. The review suggested that the performance of bonded connections can be improved through the addition of filler in the adhesive. These available studies in the literature indicate that though research work has been conducted to investigate various aspects of the BFM, the behavior of the bond layer has not been explored in detail.

In this study, X-direction is taken along the width, Y-direction is taken along the depth, and Z-direction is taken along the length of the BFM, as shown in Fig. 1. The ratio of the applied load and the failure load resisted by the BFM is termed as load proportion factor (LPF).

This study numerically investigates effect of various parameters on the behavior of the bond layer in BFMs in terms of variation of (a) normal stress, σ_y^+ , (b) normal strain, ε_y^+ , (c) shear stress, τ_{yz} , and (d) shear strain, γ_{yz} , along the length. The behavior of the bond layer is studied for parameters: (a) LPF, (b) longitudinal distribution of load, (c) transverse distribution of load, (d) width of concrete slab, B_c , (e) depth of the concrete slab, D_c , (f) Young's modulus of adhesive, E_A , and (g) transverse location of adhesive fiber. To conduct the study, a three-dimensional (3D) finite element (FE) model of BFM is developed. The observations are made at the mid-depth of the bond layer, whose coordinates are $(x, D_c + 0.50 D_a, z)$, where D_c = depth of concrete slab, D_a = depth of bond layer, x = distance along width of cross-section from mid-width, and z = distance along longitudinal direction from mid-span, as shown in Fig. 1a, b. Mid-width ($x/B_a = 0.00$) and the coordinate system followed are also shown in Fig. 1b, where B_a = width of the bond layer.

2 Finite Element Modeling of Bonded Flexure Members

Thirteen BFMs, BFM1–13, are considered for this study. All the BFMs considered in this study are symmetric in the longitudinal and transverse directions in geometry, boundary conditions, and loading. Symmetry in longitudinal and transverse directions for one typical BFM, BFM1, can be seen in Fig. 1a, b. A quarter of the BFMs in the plane is modeled by taking advantage of the symmetry. Concrete slab, bond layer, and steel girder are modeled as three-dimensional eight-node continuum elements (C3D8) elements. Reinforcement bars are modeled as two-node beam element (B21). Concrete slab, bond layer, and steel girder are modeled as a single part to reduce the numerical size of the model. Reinforcement bars are embedded in the concrete slab area of the unified part. Self-weight and external load are applied using the *Static, Riks* procedure available in Abaqus. This procedure is based on the arc length method (Riks 1979), which was proposed to obtain a solution of unstable problems. Normal stress, normal strain, shear stress, and shear strain at desired LPF are obtained by

using linear interpolation on the results obtained by the *Static, Riks* procedure.

The mesh sensitivity test is carried out during development of the numerical model. Length, width, and height of a typical C3D8 element are kept approximately equal. Convergence in terms of stress in the bond layer is achieved at 93,771 elements and 107,312 nodes in model BFM1.

Concrete is modeled using the concrete damaged plasticity (CDP) model (Lee and Fenves 1998; Lubliner et al. 1989) available in Abaqus. The stress–strain behavior of concrete is input as inelastic with strain softening CDP having an effective stress-based yield function and adopting non-associated potential plastic flow. It is capable of adequately simulating concrete behavior with the help of the uniaxial stress–strain relationship. The ratio of the second deviatoric stress invariant on the tensile meridian to that on the compressive meridian at initial crushing for any given value of effective hydrostatic stress, K_c is taken here as 0.6667, the default value suggested by the Abaqus Analysis user's manual (2013). The ratio of equibiaxial compressive strength of concrete to uniaxial cylindrical compressive strength of concrete is taken as 1.16. Yield surface of the concrete in the CDP in the deviatoric plane and plane stress are shown in Fig. 2. The value of the dilation angle measured in p–q plane is taken as 36° (Matsagar 2016). The rate at which the flow potential function reaches its asymptote is taken as 0.1, and the viscosity parameter is taken as 0 in the study, default values suggested by the Abaqus Analysis user's manual (2013). The stress–strain relationship of concrete is adopted as linear up to $0.4f_u^+$, where f_u^+ denotes the cylindrical uniaxial compressive strength of concrete. Beyond the value of $0.4f_u^+$, the stress–strain relationship for uniaxial compression proposed by Carreira and Chu (1985) is adopted, as expressed in Eq. 1 (Fig. 3).

$$\frac{\sigma^+}{f_u^+} = \frac{\gamma_C \left(\varepsilon^+ / \varepsilon_f^+ \right)}{\gamma_C - 1 + \left(\varepsilon^+ / \varepsilon_f^+ \right)^{\gamma_C}}; \gamma_C = \frac{1}{1 - \left(f_u^+ / E_{it} \varepsilon_f^+ \right)} \quad (1)$$

where E_{it} represents the initial Young's modulus of concrete, ε_f^+ represents the strain corresponding to f_u^+ , σ^+ represents the compressive stress in concrete, and ε^+ is the compressive strain in concrete. A positive superscript, in this paper, represents compression, whereas a negative superscript represents tension.

A linear stress–strain relation of stress and strain of concrete in tension is considered before and after cracking in this study, as shown in Fig. 3. The adopted relation between tensile strength of concrete, f_{cr}^- , and f_u^+ is shown in Eq. 2, which has been adopted from ACI 318 (2019).

$$f_{cr}^- = 0.62 f_u^{+1/2} \quad (2)$$

Fig. 2 Yield surface of concrete damaged plasticity in **a** deviatoric plane, and **b** plane stress

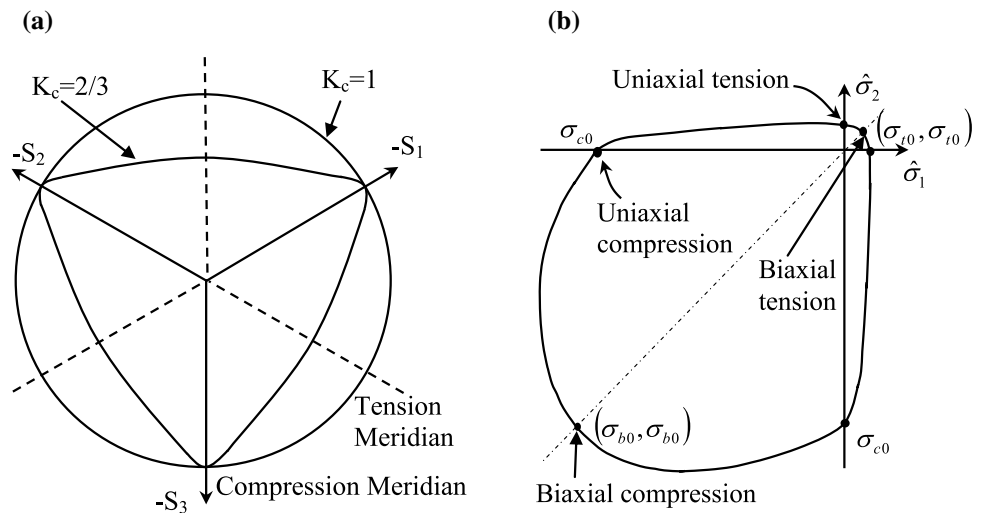
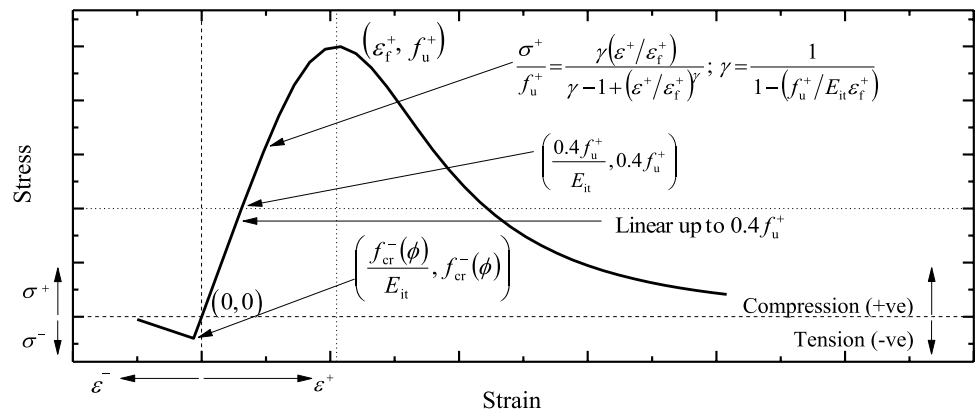


Fig. 3 Uniaxial stress–strain curve for concrete, compression as positive and tension as negative



This relationship is prescribed as the upper limit of tensile stress for uncracked concrete in ACI 318 (2019). The value of f_{cr}^- using Eq. 2 has been obtained as 4.0 MPa.

The adhesive is modeled using the linear Drucker–Prager (LDP) material model (Chiang and Herzl 1994; Drucker and Prager 1952) with the associated flow. Structural steel is modeled as multi-linear plastic material, and reinforcement is modeled as bi-linear plastic material with the isotropic hardening model. Figure 4a shows the mesh of a typical BFM, BFM1, along with loading and the boundary conditions. Figure 4b shows the deflected shape of the FE model of BFM1. The deformation is magnified at a scale of 10.

The FE model is validated against experimental results of the beam P_1 tested by Bouzaoui et al. (2007) (Fig. 5a,b), designated here as the validation BFM VB1, experimental results of the beam B4 tested by Souici et al. (2013) (Fig. 5c, d), designated here as the validation BFM VB2, and experimental results of the beam AB1 tested by Jurkiewicz et al. (2011) (Fig. 5e, f), designated here as the validation BFM VB3. All the three validation BFMs are symmetric in the plane in the lateral and transverse directions in geometry, boundary conditions and loading, which can be seen in

Fig. 5a–f. Therefore, again a quarter of the BFM in the plane is considered in the FE model. Material properties of all the three VBs are shown in Table 1. Comparison of load–displacement curves obtained by FE model with those obtained by experimental studies is shown in Fig. 5g. The comparison shows that the FE model predicts the behavior of BFM with good accuracy. Figure 6 shows the failure of VB2 observed experimentally by Souici et al. (2013). Figure 6 also shows prediction of failure obtained using the developed numerical model, which is similar to the observed failure. It can be stated that the numerical model is reliable.

3 Numerical Study and Discussion

For BFM1, Young’s modulus, compressive strength, and tensile strength of concrete are 30,314 MPa, 41.6 MPa, 4.0 MPa, respectively. Young’s modulus of adhesive, E_A , compressive strength, and tensile strength of adhesive are 12,300 MPa, 55 MPa, and 30 MPa, respectively. Young’s modulus, Poisson’s ratio and yield stress of steel I-section are 210,000 MPa, 0.3, and 500 MPa, respectively. Young’s

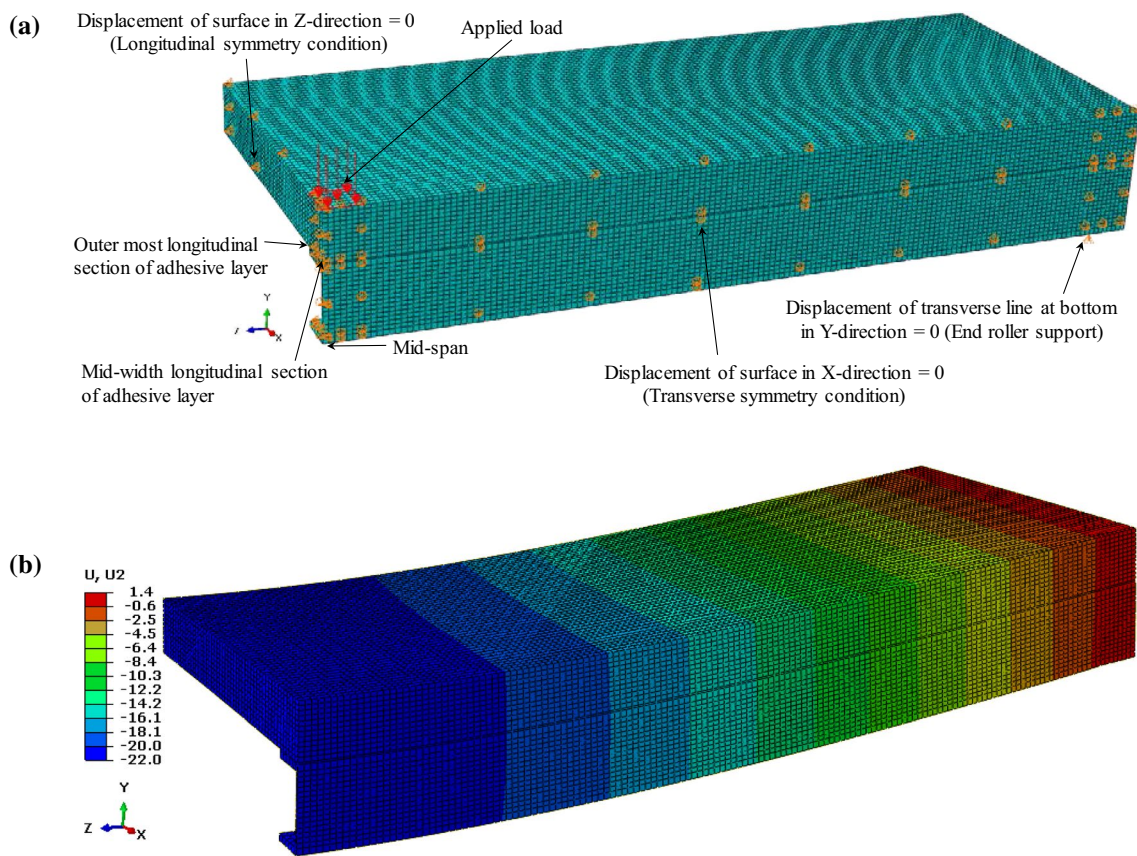


Fig. 4 Modeling of BFM1: **a** mesh and boundary conditions, modelled quarter in plan, and **b** deflected shape, with magnified deformation at scale of 10

modulus, Poisson’s ratio, and yield stress of steel reinforcement are 210,000 MPa, 0.3, and 325 MPa, respectively. BFM1 is adopted from the shear stud connected steel–concrete beam B4 tested by Amadio et al. (2004).

3.1 Effect of load proportion factor (LPF)

Effect of LPF on the normal stress, normal strain, shear stress, and shear strain is presented in this section. Details of BFM1 can be seen in Fig. 1. Figure 7 shows the comparison among variations in these quantities at the mid-width longitudinal section of the bond layer. Considered LPFs are 0.40, 0.60, 0.80, 0.90, 0.95, and 1.00. Normal stress at the location of the applied load increases with the increase in LPF from LPF = 0.40 to 0.60, as shown in Fig. 7a. On the contrary, normal stress decreases with increase in LPF for LPF > 0.60. Normal strain, on the other hand, keeps increasing till LPF = 1.00 (Fig. 7b). Further, it is observed that normal strain is highest for LPF = 1.00 for most of the length while normal stress is highest only at support. The BFM is simply supported with load applied at mid-span. Therefore, the bond layer experiences maximum magnitude of longitudinal bending strain, ϵ_z , and stress, σ_z ,

at mid-span and almost zero at support. In the considered case, longitudinal bending tensile strain, ϵ_z^- , is 161 μ and 1102 μ at LPF = 0.40 and 1.00, respectively, at mid-span while longitudinal bending tensile strain is 35 μ and 244 μ at LPF = 0.40 and 1.00, respectively, at support. Magnitude of longitudinal bending strain and transverse strain, ϵ_x , affects the magnitude of normal stress as expressed in Eq. 3 (Timoshenko and Goodier 2010).

$$\sigma_z^+ = \frac{E}{(1 + \nu)(1 - 2\nu)} [\nu\epsilon_x + \nu\epsilon_y + (1 - \nu)\epsilon_z] \quad (3)$$

High magnitude of longitudinal bending tensile strain causes a lower magnitude of normal stress at LPF = 1.00 in the span (Eq. 3). On the contrary, BFM at support experiences support reaction but negligible longitudinal bending tensile strain, due to which high normal stresses are developed in the bond layer. It has been observed that both normal stress and normal strain have a peak at support.

Variations of shear stress and shear strain are shown in Fig. 7c, d, respectively. Variation of shear stress is similar to the variation of shear strain through the length at each LPF. At LPFs > 0.40, shear stress and shear strain are

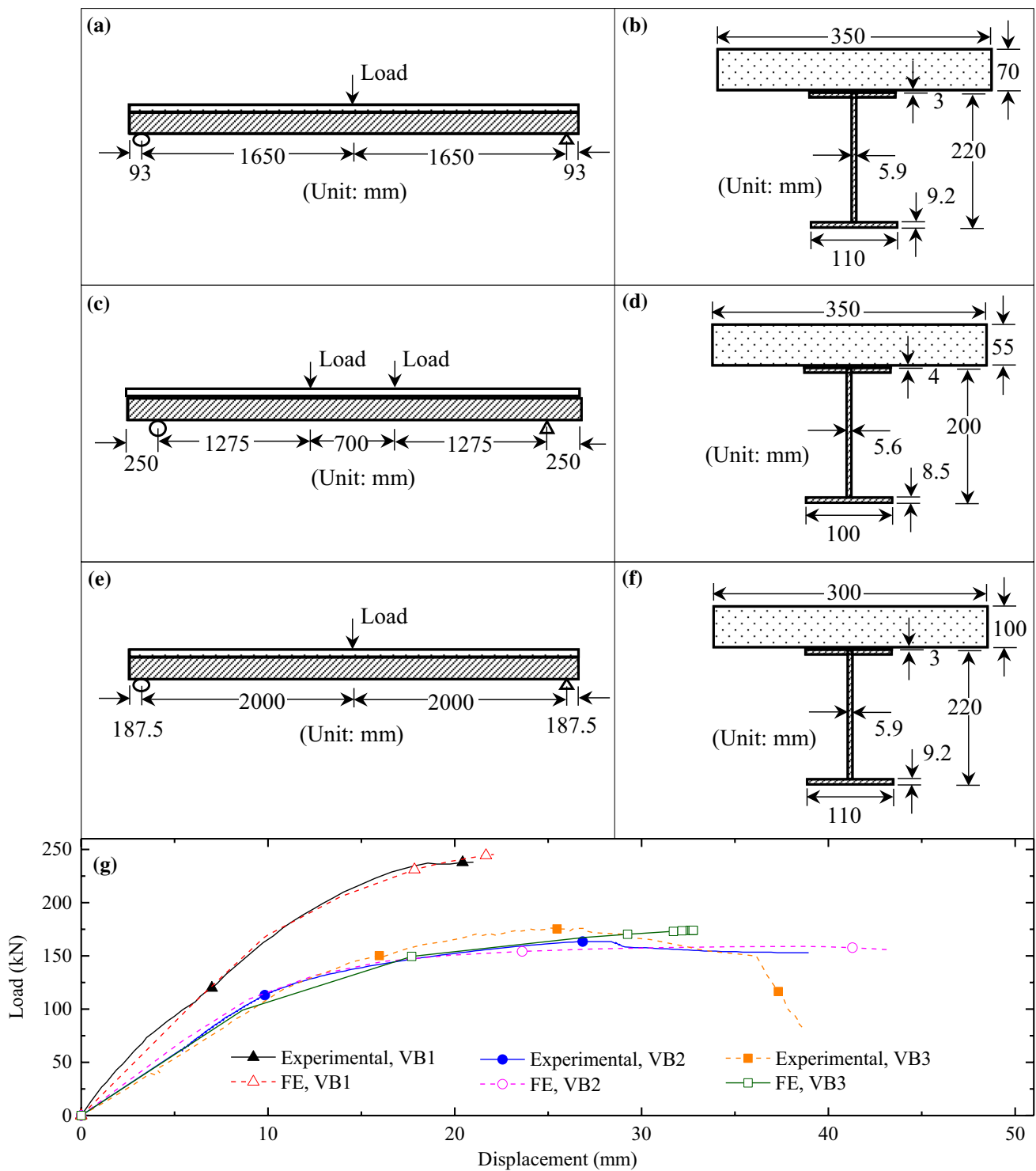


Fig. 5 Validation of the FE model: **a** side view of VB1, **b** cross-sectional view of VB1, **c** side view of VB2, **d** cross-sectional view of VB2, **e** side view of VB3, **f** cross-sectional view of VB3 and **g** Com-

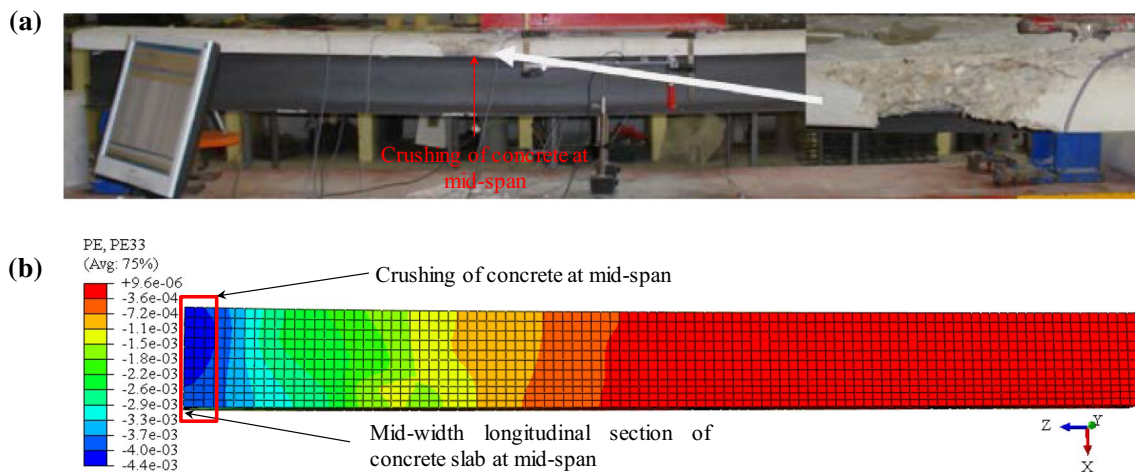
parison of mid-span deflections of VB1, VB2 and VB3 obtained by FE model and experimental studies

larger at mid-span and at support than at other locations creating local peaks. Maximum shear stress in the bond layer is found beneath the applied load and at supports at

failure load. As discussed earlier, local peaks of normal stress and normal strain are also observed at the same locations. These peaks become sharp at LPF = 1.00. It can be

Table 1 Material properties of all the three VBs

	Cylindrical uniaxial compressive strength of concrete, f_u^+ (MPa)	Uniaxial tensile strength of concrete, f_{cr}^- (MPa)	Young's modulus of adhesive, E_A (MPa)	Uniaxial tensile strength of adhesive, $f_{u,a}$ (MPa)	Young's modulus of steel I-section, E_s (MPa)	Yield stress of steel I-section, f_{ys} (MPa)
VB1	68	4.0	12,300	19.5	205,000	470
VB2	35	4.0	12,300	15	210,000	235
VB3	39	4.0	12,300	19.5	210,000	275

**Fig. 6** Comparison of failure of VB2 **a** observed experimentally by Souici et al. (2013) and **b** obtained numerically

stated that high values of normal strain and high values of shear stress and shear strain occur simultaneously. This is supported by Fig. 7 for all LPFs, which shows the presence of higher values of normal strain and peaks in shear stress and shear strain simultaneously.

Variation in shear force is compared with variation in shear stress at LPF = 0.40 to understand the applicability of classical beam theory on BFM in this study. Classical beam theory assumes that the deflection in the flexural member is small compared to its span and the plane section normal to the longitudinal axis before bending remains planar after bending. Classical beam theory does not consider any slip between two elements of a beam. Further, shear stress is directly proportional to shear force at the cross-section. Therefore, similarity of the shear force profile using classical beam theory with the shear stress profile indicates negligible slip and high or near full interaction. In other words, it shows good composite action.

For BFM1, variation of shear stress (Fig. 7c) at LPF = 0.40 is similar to the variation of shear force (Fig. 8) obtained using classical beam theory. Therefore, classical beam theory can be stated to be applicable on BFM1, i.e. BFM1 exhibits a near full or high degree of interaction.

3.2 Effect of longitudinal variation in loading arrangement

Three different loading arrangements are applied on BFM to study the effect of longitudinal variation in loading arrangements on the behavior of the bond layer. The loading arrangements are mid-span mid-width patch loading arrangement (LA = 1, BFM1), two-position mid-width patch loading arrangement (LA = 2, BFM2), and full-length mid-width strip loading arrangement (LA = 3, BFM3), as shown in Fig. 9a. Figure 9b–e show a comparison among variations in normal stress, normal strain, shear stress, and shear strain at the mid-width longitudinal section of the bond layer of BFM. All the geometrical and material properties of the BFM2–3 are the same as BFM1. Among the three BFMs, BFM3 resists maximum load (785.2 kN) while BFM1 resists minimum load (580.3 kN) at failure.

BFM1 exhibits highest normal stress and normal strain at LPF = 0.40 and 1.00 at mid-span which is beneath the applied load (Fig. 9b, c). Similarly, BFM2 exhibits highest normal stress and normal strain beneath the load ($z/L_0 = 0.13$) at LPF = 0.40 and 1.00. At all other points along the length, BFM3 exhibits the highest normal stress and normal strain. BFM with full-length mid-width strip loading

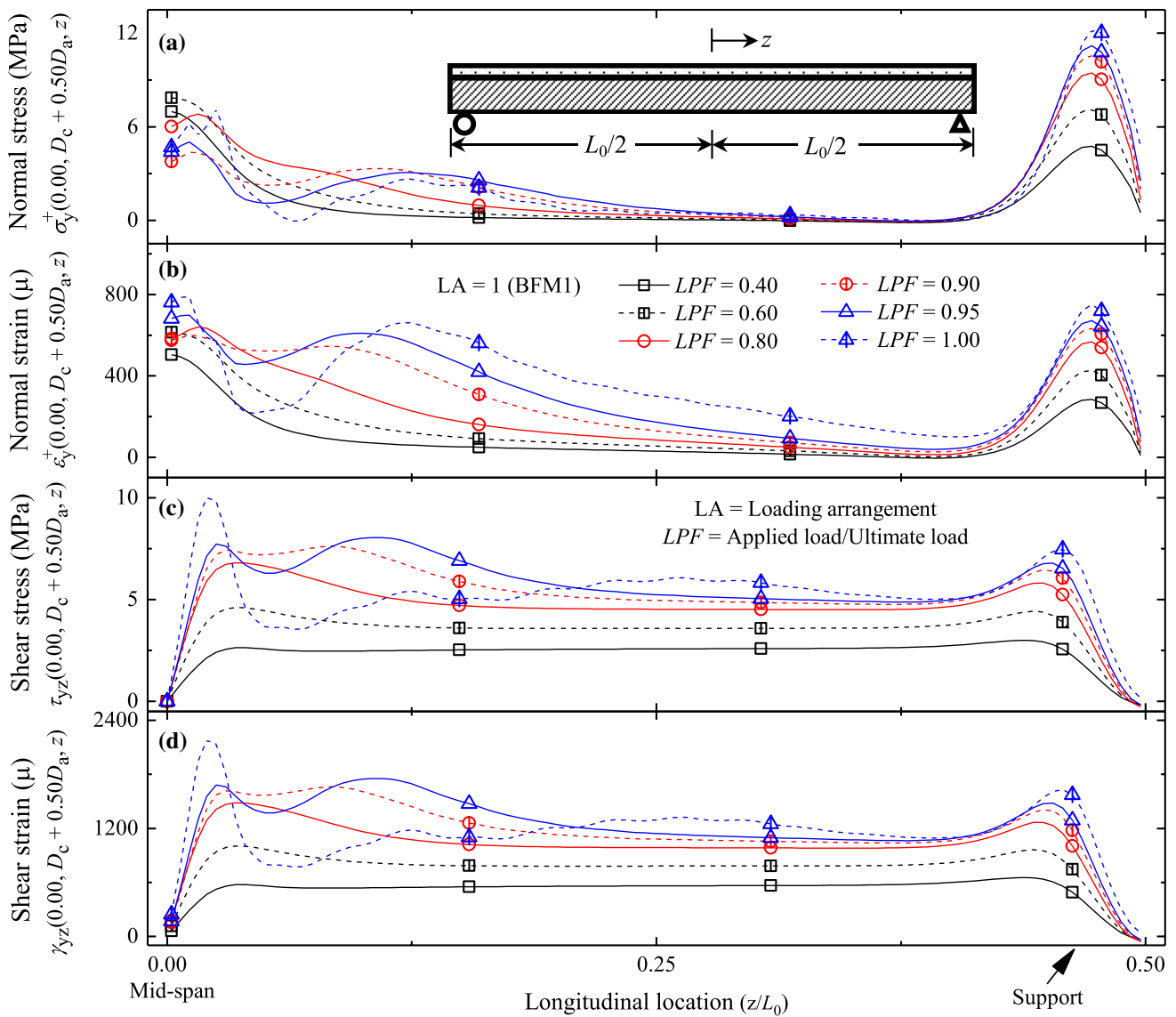
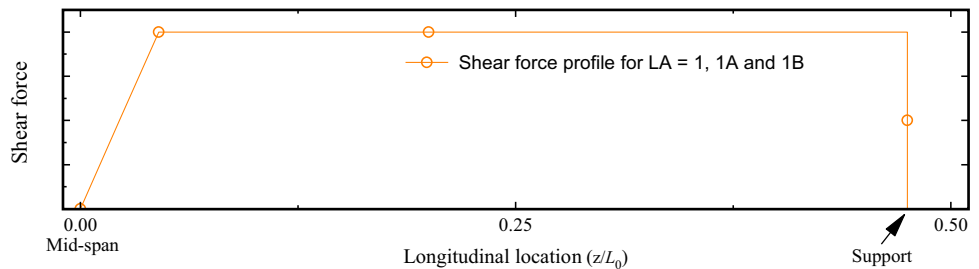


Fig. 7 Variations of considered parameters at mid-width longitudinal section of the bond layer of BFM1 along the length at different LPFs: **a** normal stress, **b** normal strain, **c** shear stress, and **d** shear strain

Fig. 8 Variations of shear force along the length for loading arrangements LA = 1, 1A and 1B



arrangement, BFM3, experiences abnormally high normal stress and normal strain at support as the bond layer experiences imposed loading and high support reaction at the same location. Normal stress experienced by the bond

layer of BFM3 at support is 74.4 times the normal stress at mid-width. Normal stress experienced by the bond layer of BFM3 is 3.92 times the normal stress experienced by the bond layer of BFM1 at support.

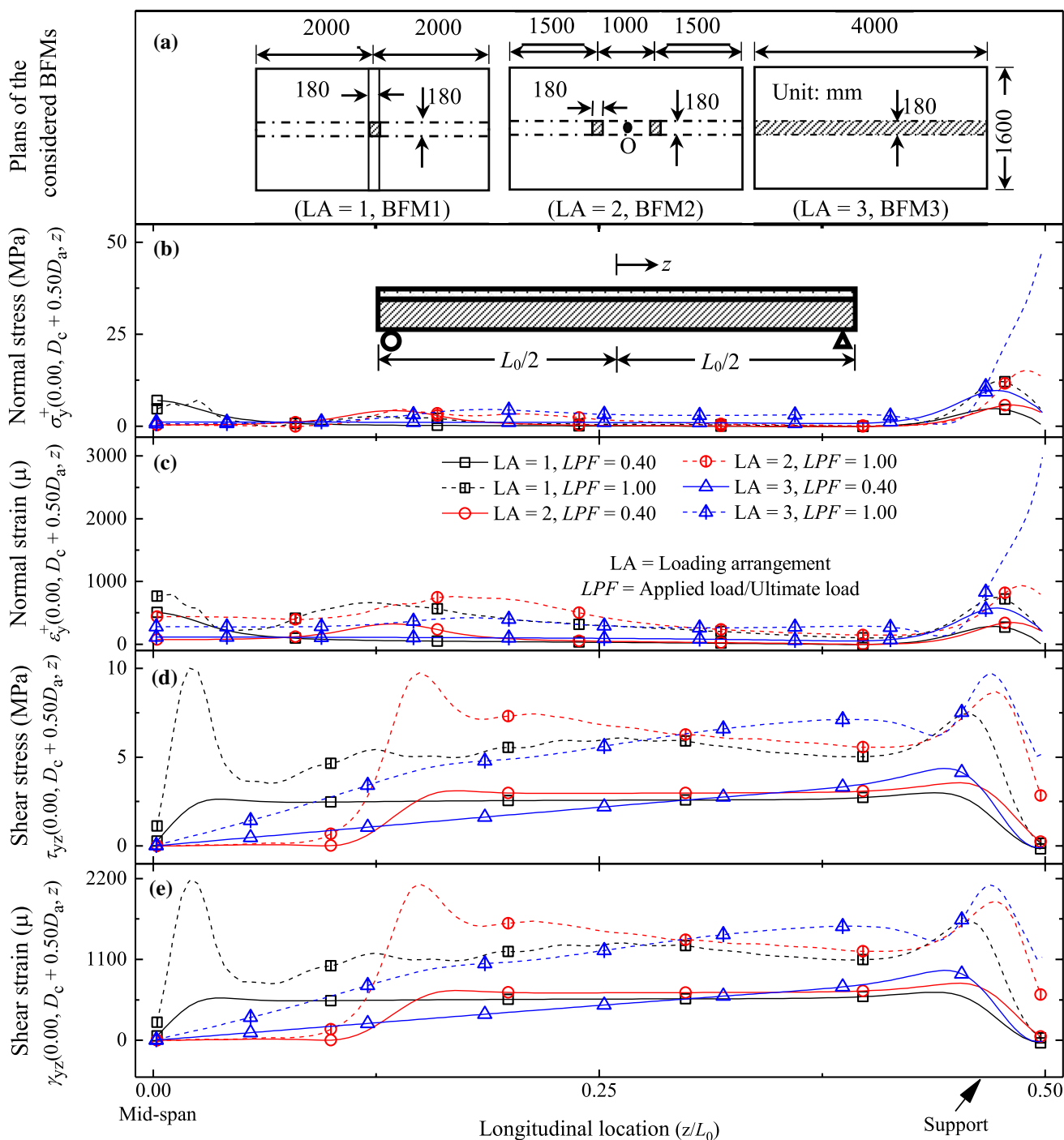


Fig. 9 Variations of considered parameters at mid-width longitudinal section of the bond layer along the length: **a** plans of BFMs, **b** normal stress, **c** normal strain, **d** shear stress, and **e** shear strain

Variations of shear stress and shear strain are similar for each case (Fig. 9d, e). At mid-span, BFM1 exhibits the highest shear stress at LPF=0.40 and 1.00. As a patch load is applied in a small area at mid-span in BFM1, it causes high normal strain and stress at the location of the patch load at LPF=1.00. A sharp peak in shear stress is also observed at

the same location. Similarly, BFM2 exhibits a sharp peak in shear stress at LPF=0.40 and 1.00, at the location of the applied patch load, $z/L_0=0.13$. At all other points, BFM3 exhibits the highest shear stress for each LPF. Therefore, the effect of normal forces on the shear stress is evident beneath the load and supports in all the BFMs at LPF=1.00.

The variation profile of shear stress at $LPF=0.40$ is similar to the variation profile of shear force obtained using classical beam theory (Fig. 10) along the length, for each loading arrangement. As discussed in Sect. 3.1, similarity of the shear force profile using classical beam theory with the shear stress profile indicates high degree of interaction. It is clear that the classical beam theory is applicable on BFM1-3. Therefore, it can be stated that BFM1-3 exhibit high degree of interaction.

3.3 Effect of transverse variation in loading arrangement

Three different loading arrangements are applied on BFM to study the effect of transverse variation in loading arrangement on the behavior of the bond layer. The loading arrangements are mid-span mid-width patch loading arrangement ($LA=1$, BFM1), mid-span full-width strip loading arrangement ($LA=1A$, BFM4), and mid-span outer-width strip loading arrangement at mid-span ($LA=1B$, BFM5), as shown in Fig. 11a. Figure 11b–e show a comparison among variations in normal stress, normal strain, shear stress, and shear strain at the mid-width longitudinal section of the bond layer of BFM. All the geometrical and material properties of the BFM4-5 are the same as BFM1. Among the three BFMs, BFM1 resists maximum load (580.3 kN) while BFM3 resists minimum load (458.6 kN) at failure.

As a patch load is applied at mid-span, BFM1 exhibits its highest values of normal stress and normal strain at $LPF=0.40$ and 1.00 at mid-span underneath the patch load (Fig. 11b, c). While BFM4-5 experiences tensile normal stress $\sigma_y(0.00, D_c + 0.50 D_a, z)$ at mid-span at $LPF=1.00$. The maximum value of normal tensile stress in BFM4 and BFM5 are 2.10 and 2.31 MPa, respectively, which are significantly lower than the tensile strength of the adhesive. The transverse distance of the load from the bond layer induces tensile stress at mid-span in BFM4-5. Tensile stress vanishes at sections far from the mid-span. Normal strain and stress in the bond layer of BFM1 are slightly greater than BFM4-5 at the support level.

Variations of shear stress and shear strain are similar for all the three BFMs (Fig. 11d, e) at $LPF=0.40$ except sections near mid-span. At mid-span, BFM1 exhibits the highest

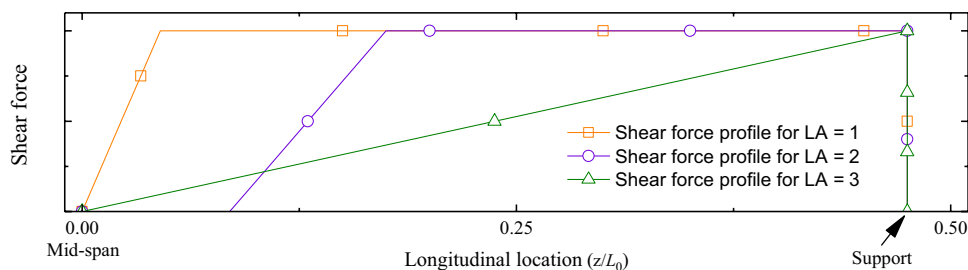
shear stress at $LPF=0.40$ and 1.00 . At $LPF=1.00$, variation in the shear stress and shear strain profile of BFM4-5 does not exhibit any sharp peak at mid-span, which can be attributed to the load being applied over a larger area compared to BFM1. Local peaks of shear stress and shear strain are observed at the location of high normal strain. This happens due to the influence of high normal stress on shear stress and shear strain beneath the load and at support in the bond layer.

The variation profile of shear stress (Fig. 11d) in BFM4-5 at $LPF=0.40$ is similar to the variation profile of shear force obtained by classical beam theory (Fig. 8), which indicates applicability of classical beam theory and high degree of interaction. However, little difference in the variation profile of shear stress in BFM4-5 at $LPF=0.40$ and the variation profile of shear force obtained by classical beam theory is observed near mid-span. This indicates a change in the load transfer path as the load is away from mid-width in BFM4-5. The shear force develops fully in the bond layer exactly below the load in BFM1 where the load is applied exactly above the bond layer. On the other hand, the shear force develops fully at a small distance from load in the bond layer in BFM4-5 where the load is applied at locations transversely away from the bond layer.

3.4 Effect of width of concrete slab

Effect of width of concrete slab on bond layer of BFM is studied on four BFM with different width of the concrete slab (B_c), i.e., 1600 mm (BFM1), 3800 mm (BFM6), 950 mm (BFM7), and 475 mm (BFM8), as shown in Fig. 12a. All other geometrical and material properties of the BFM6-8 are the same as BFM1. Among the four BFMs, BFM6 resists maximum load (499.8 kN) while BFM8 resists minimum load (351.1 kN) at failure. Figure 12b–e show a comparison among variations in normal stress, normal strain, shear stress, and shear strain at the mid-width longitudinal section of the bond layer of BFM. Normal stress and normal strain at mid-span at $LPF=0.40$ are highest for the BFM with $B_c=3800$ mm and lowest for the BFM with $B_c=475$ mm (Fig. 12b, c), which can be attributed to the difference in the failure load resisted by the BFMs. At $LPF=1.00$, normal stress decreases for all the BFMs, compared to normal stress at $LPF=0.40$. At support, normal stress is

Fig. 10 Variations of shear force along the length for loading arrangements $LA=1$, 2 and 3



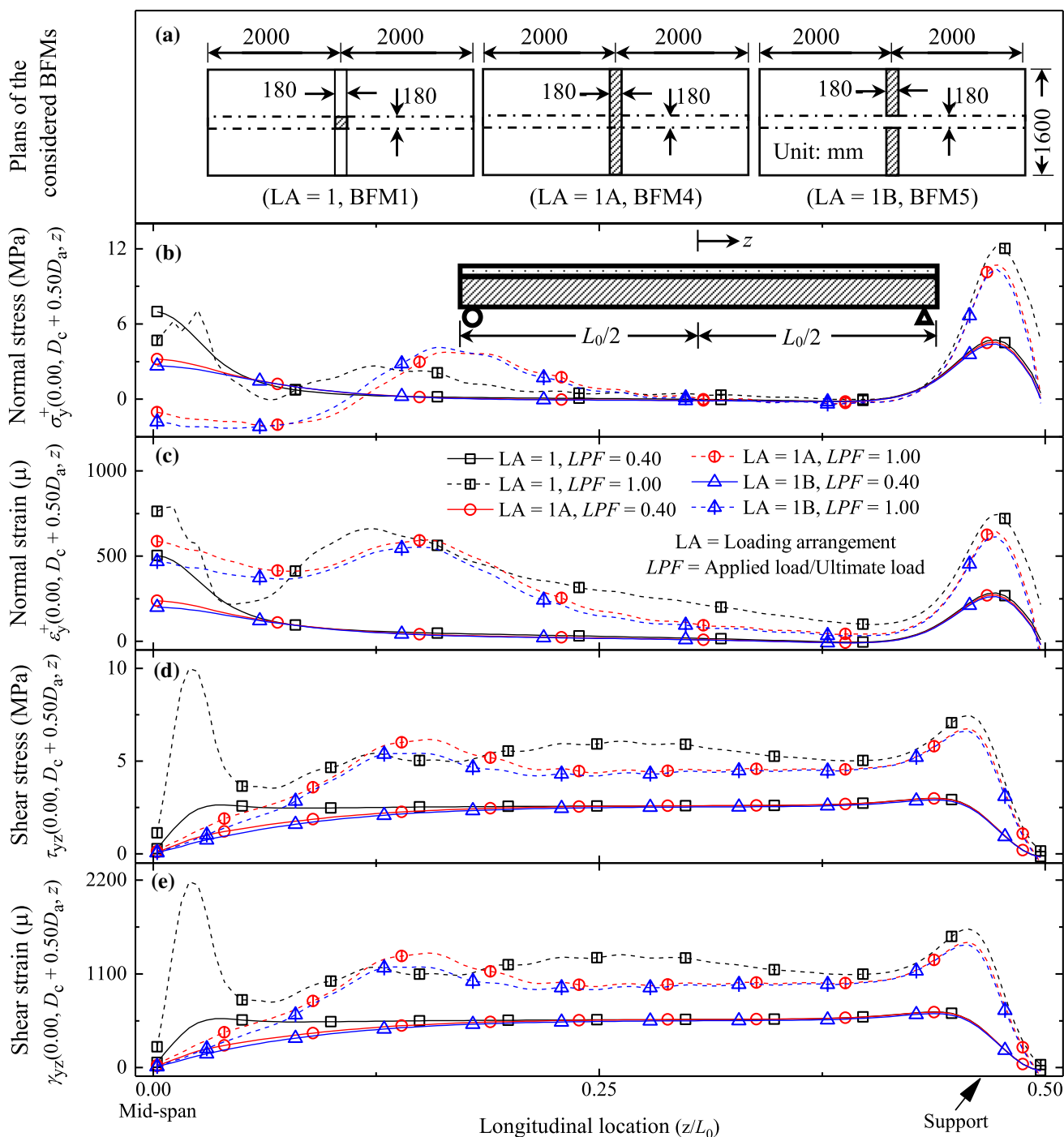


Fig. 11 Variations of considered parameters at mid-width longitudinal section of the bond layer along the length: **a** plans of BFMs, **b** normal stress, **c** normal strain, **d** shear stress, and **e** shear strain

highest for the BFM with $B_c = 3800$ mm and lowest for the BFM with $B_c = 475$ mm at both LPFs.

The variation of shear stress is similar to the variation of shear strain for each case (Fig. 12d, e). Shear strain is highest for the BFM with $B_c = 3800$ mm and lowest for the BFM with $B_c = 475$ mm at both LPFs at mid-span and support.

The BFM with $B_c = 475$ mm does not exhibit a sharp peak in normal stress at mid-span at LPF = 1.00, unlike for the BFMs with $B_c = 3800$ mm, 1600 mm, and 950 mm. It is evident that the tri-axial state affects shear stress and shear strain. It was observed in previous sections that peaks in shear stress and shear strain are accompanied by peaks in

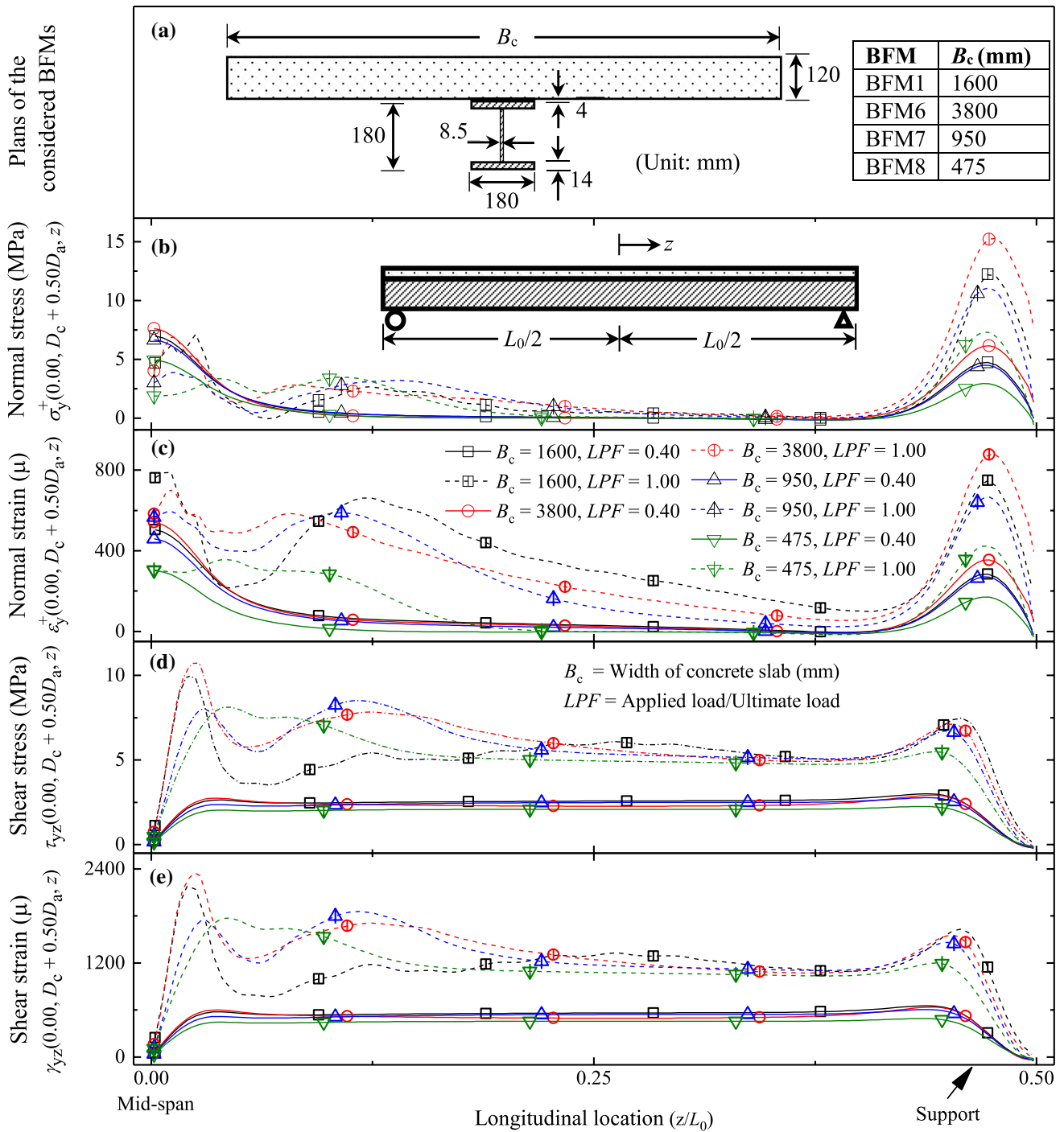


Fig. 12 Variations of considered parameters at mid-width longitudinal section of the bond layer along the length: **a** cross-sections of BFMs, **b** normal stress, **c** normal strain, **d** shear stress, and **e** shear strain

normal stress and normal strain for each case. Higher values of shear stress and shear strain are found at the location of the higher value of normal stress and normal strain. In the case of the BFM with $B_c = 475$ mm, the absence of a sharp peak in normal stress and the absence of a sharp peak in shear stress at mid-span at $LPF = 1.00$ are observed.

This absence of a peak in shear stress, in turn, results in the absence of stress depression for the BFM with $B_c = 475$ mm near mid-span at $LPF = 1.00$. On the contrary, stress depression near mid-span at $LPF = 1.00$ can be seen in case of the BFMs with $B_c = 3800$ mm, 1600 mm, and 950 mm at the end of the load area ($z/L_0 = 0.045$), to maintain the shear

flow. Smaller width of concrete slab leads to a smooth variation of shear stress and shear strain profile at failure load except at supports. Shear stress is highest for the BFM with $B_c = 1600$ mm and lowest for the BFM with $B_c = 475$ mm at both LPFs at support.

For the considered BFMs, the variation of shear stress at $LPF = 0.40$ is similar to the variation of shear force (Fig. 8) obtained using classical beam theory. Therefore, the considered BFMs exhibit a near full or high degree of interaction.

3.5 Effect of depth of concrete slab

Effect of depth of concrete slab on the bond layer of BFM is studied on three BFM with different depth of concrete slab (D_c), i.e., 120 mm (BFM1), 210 mm (BFM9), and 300 mm (BFM10), as shown in Fig. 13a. All other geometrical and material properties of the BFM9-10 are the same as BFM1. Among the three BFMs, BFM10 resists maximum load (907.2 kN) while BFM1 resists minimum load (481.3 kN) at failure. Peak normal stress and normal strain at $LPF = 0.40$ decrease with increase in the depth of concrete slab despite an increase in failure load with the increase in the depth of concrete slab (Fig. 13b, c). This can be attributed to the increased area of load disbursement at the level of adhesive due to the greater depth and greater stiffness of concrete slab. At $LPF = 1.00$, the BFM with $D_c = 120$ mm shows highest and the BFM with $D_c = 210$ mm shows lowest normal stress under the load. On the other hand, the BFM with $D_c = 210$ mm undergoes highest normal strain at $LPF = 1.00$ under the load. This behavior is due to the combined effect of higher values of failure load, load disbursement area at the bond level and stiffness of concrete slab. At support, the BFMs with $D_c = 210$ mm and 300 mm experience abnormally high normal stress and normal strain due to high support reaction and high stiffness of concrete slab.

The variation in shear stress (Fig. 13d) is similar to the variation in shear strain (Fig. 13e) for each LPF. The BFM with $D_c = 120$ mm exhibits a sharp peak in shear stress at $LPF = 1.00$. It is also observed that higher depth of concrete slab lead to a smooth variation of shear stress and shear strain profile at failure load except at supports. Though load resisted by the three BFMs differs greatly, shear stress does not differ considerably. This happens due to the combination of increase in the failure load, increase in stiffness of BFM and upward shifting of the neutral axis with increase in the depth of the concrete slab. Increase in the failure load increases the shear flow in the BFM at failure. On the other hand, increase in stiffness of BFM and upward shifting of the neutral axis causes reduction in shear flow at the level of the bond layer.

For the considered BFMs, the variation of shear stress at $LPF = 0.40$ is similar to the variation of shear force (Fig. 8) obtained using classical beam theory. Therefore,

the considered BFMs exhibit a near full or high degree of interaction.

3.6 Effect of Young's modulus of adhesive

Geometric details of the BFMs considered to study the effect of Young's modulus of adhesive on the behavior of the bond layer are shown in Fig. 14a. The geometric and material details of all BFMs considered in this section are the same as BFM1 except variation in Young's modulus of adhesive (E_A) of 12,300 MPa (BFM1), 1230 MPa (BFM11), 123 MPa (BFM12), and 12.3 MPa (BFM13). It is noteworthy that experiments on epoxy-based and polyurethane-based adhesive to bond structural steel and concrete have been conducted (Bouazaoui et al. 2007; Si Larbi et al. 2007). These studies reported that epoxy-based adhesives have high Young's modulus ($E_A = 12,300$ MPa) whereas polyurethane-based adhesives have low Young's modulus ($E_A = 80$ MPa). Figure 14b–e show a comparison among variations in normal stress, normal strain, shear stress, and shear strain at the mid-width longitudinal section of the bond layer of the considered BFMs. Other than Young's modulus of adhesive, all other geometrical and material properties of the BFM11-13 are the same as BFM1. Failure loads of BFM1, BFM11, BFM12, and BFM13 obtained from FE analysis are 481.3 kN, 460.9 kN, 468.8 kN, and 397.7 kN, respectively. Peak normal stress at $LPF = 0.40$ and 1.00 decreases with a decrease in the Young's modulus of adhesive as BFMs with lower Young's modulus of adhesive experienced more evenly distributed stresses with lesser peaks and troughs (Fig. 14b). On the other hand, it is seen in Fig. 14c that the peak normal strain increases with a decrease in Young's modulus of adhesive. This can be attributed to the low axial stiffness of adhesive in BFM12-13 allowing load disbursement over a larger area at the level of adhesive reducing peak stress.

The variation of shear stress is similar to the variation of shear strain at $LPF = 0.40$ for each BFM while local peaks of shear stress are observed at support and beneath the load for BFM1 and BFM11 at $LPF = 1.00$ (Fig. 14d-e). These peaks are sharper for higher Young's modulus of adhesive, which is in a similar pattern to the normal stress. On the contrary, local peaks of shear stress are absent for BFMs with lower Young's modulus of adhesive (BFM12-13) at $LPF = 1.00$. It is also noteworthy that the peak values of shear stress of BFM12-13 are also smaller than those of BFM1,11. The presence of local peaks in shear stress in BFM1,11 and the absence of local peaks in shear stress in BFM12-13 indicate that the shear stress is strongly affected by normal stress at ultimate load.

The variation of shear stress is similar to the variation of shear force (Fig. 8) for each BFM with higher Young's modulus of adhesive i.e. $E_A = 12,300$ MPa and 1230 MPa,

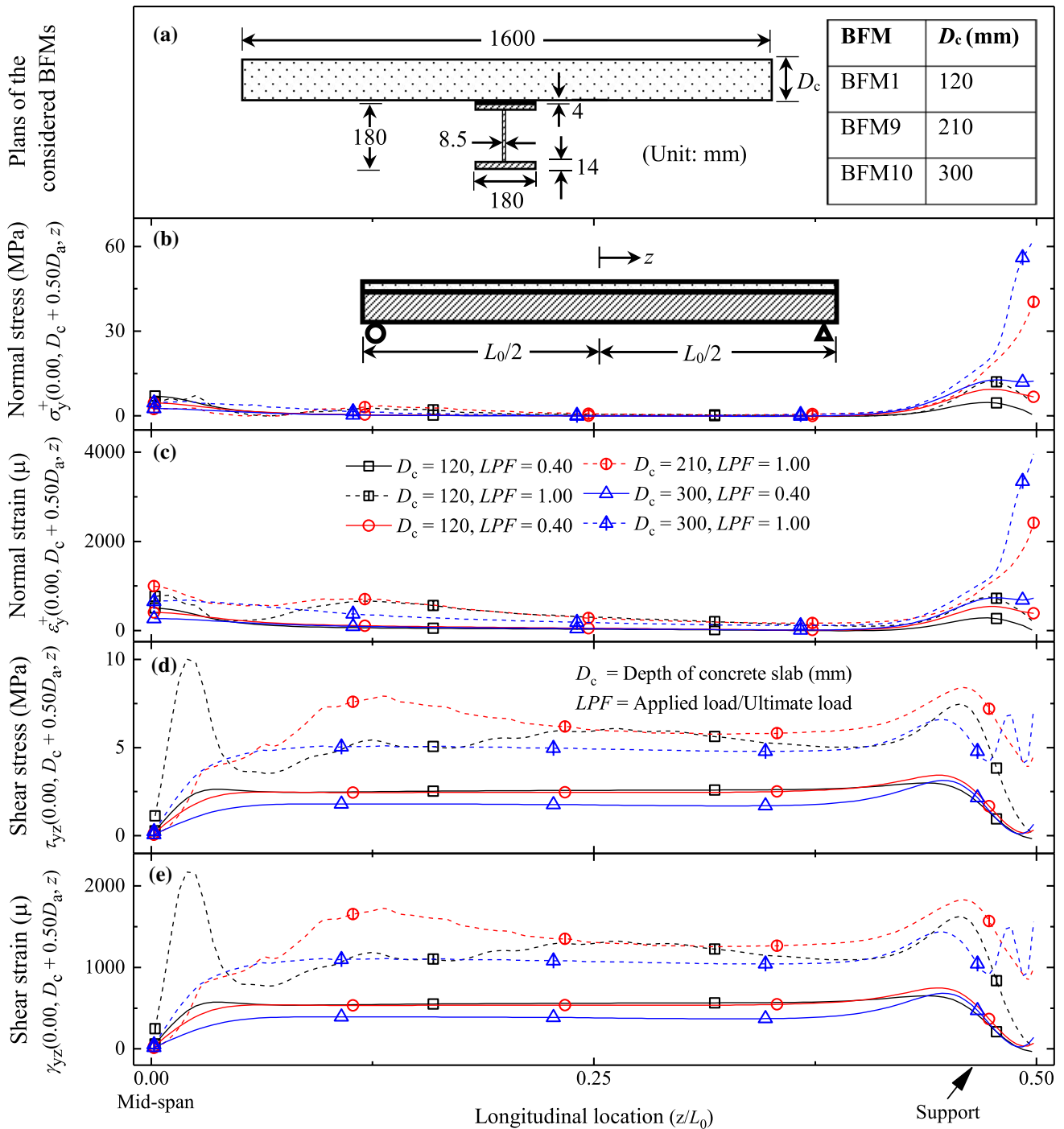


Fig. 13 Variations of considered parameters at mid-width longitudinal section of the bond layer along the length: **a** cross-sections of BFMs, **b** normal stress, **c** normal strain, **d** shear stress, and **e** shear strain

which indicates a high degree of interaction provided by these adhesives. Therefore, it can be stated that a high degree of interaction can be achieved by epoxy-based adhesive. The variation of shear stress is found to differ from the variation of shear force in the BFM obtained from classical beam theory for lower values of Young’s modulus of adhesive i.e.

$E_A = 123$ and 12.3 MPa. This indicates that the variation of the shear stress in the bond layer does not follow classical beam theory at lower values of Young’s modulus of adhesive, i.e. $E_A < 123$ MPa. This behavior can be attributed to a lower degree of interaction leading to imperfect composite beam behavior at lower values of Young’s modulus of

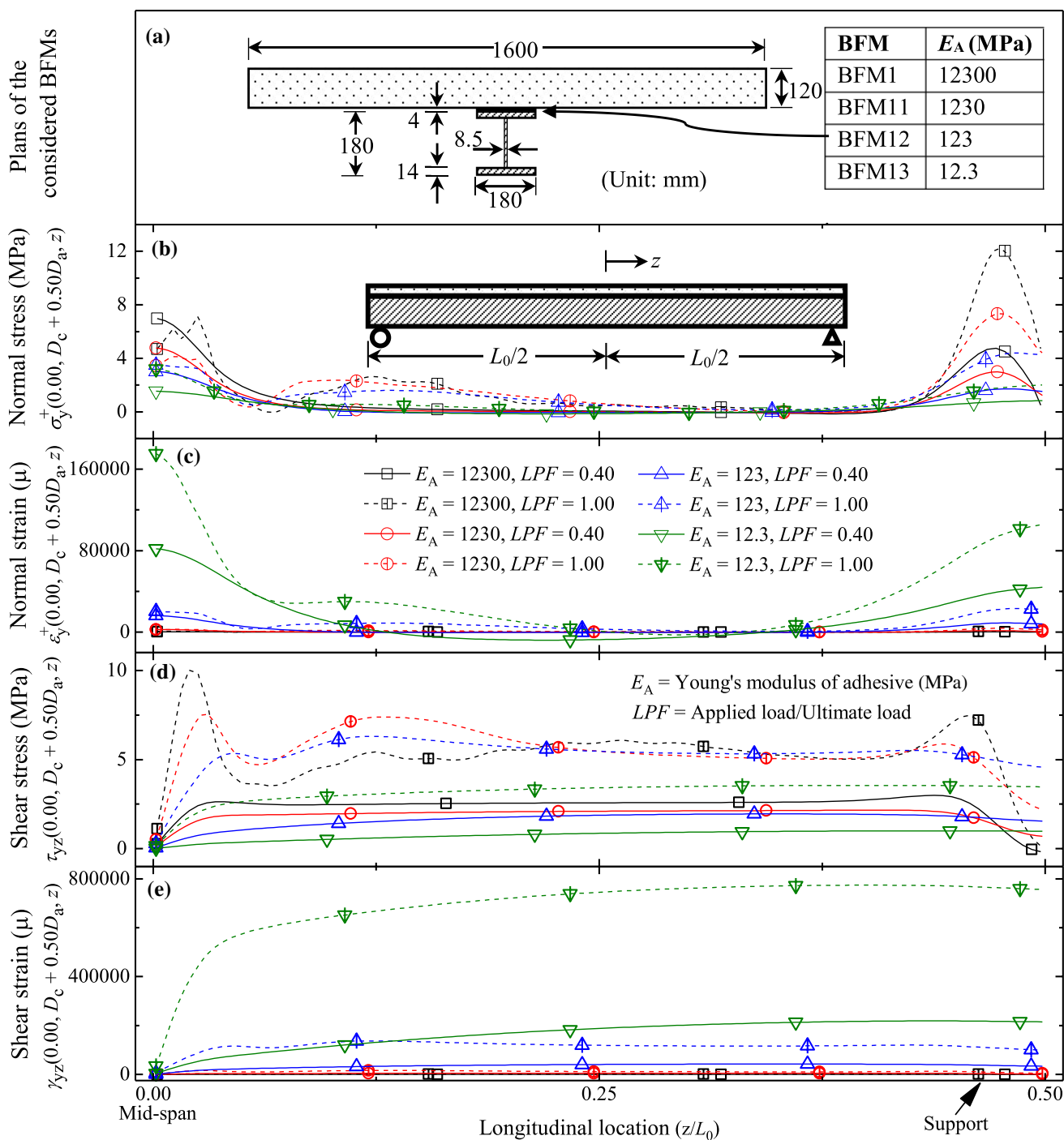


Fig. 14 Variations of considered parameters at mid-width longitudinal section of the bond layer along the length: **a** cross-sections of BFMs, **b** normal stress, **c** normal strain, **d** shear stress, and **e** shear strain

adhesive. Shear stress varying all over the length is observed for mid-span loading for lower values of Young’s modulus of adhesive ($E_A = 12.3$ MPa).

The effect of variation in Young’s modulus of adhesive on the behavior of bond layer is substantial. Young’s modulus of adhesives is seriously affected by temperature (Dai et al.

2013; Gao et al. 2012; Da Silva and Adams 2005). It is noteworthy that BFMs may experience significant variation in temperature in lifetime due to exposure to fire. Reduction in E_A in such conditions may lead to failure of BFMs. Therefore, the effect of temperature on behavior of BFM should be understood in detail before adopting them in practice.

3.7 Variation of stress and strain along the transverse fiber of adhesive bond layer

Variations of normal stress, normal strain, shear stress, and shear strain at three different longitudinal sections of bond layer of BFM are studied on BFM1 at LPFs = 0.40 and 1.00 for three different longitudinal sections, viz. mid-width ($x/B_a = 0.00$), quarter-width ($x/B_a = 0.25$) and outer longitudinal section ($x/B_a = 0.50$), as shown in Fig. 15. At mid-span, normal stress is highest at mid-width at LPF = 0.40 (Fig. 15a). Most of the area of the bond layer is under compression, but significant normal tensile stress is observed at the outer longitudinal section. The presence of longitudinal

tensile stress in the unconfined outer longitudinal section causes tensile normal stress. A similar pattern is observed at LPF = 1.00, though compressive stress reduces and tensile stress increases in respective areas. Peaks are observed in normal stress at supports due to support reaction. It is observed that the normal stress in the mid-width longitudinal section is highest and normal stress in the outer longitudinal section is lowest among the three considered locations. Similar behavior is observed for normal strains (Fig. 15b).

The variations of shear stress and shear strain are shown in Fig. 15c, d, respectively. The variation of shear stress is similar to the variation of shear strain through the length at both LPF = 0.40 and 1.00. Shear stress in mid-width and the outer longitudinal section is found to be higher while shear

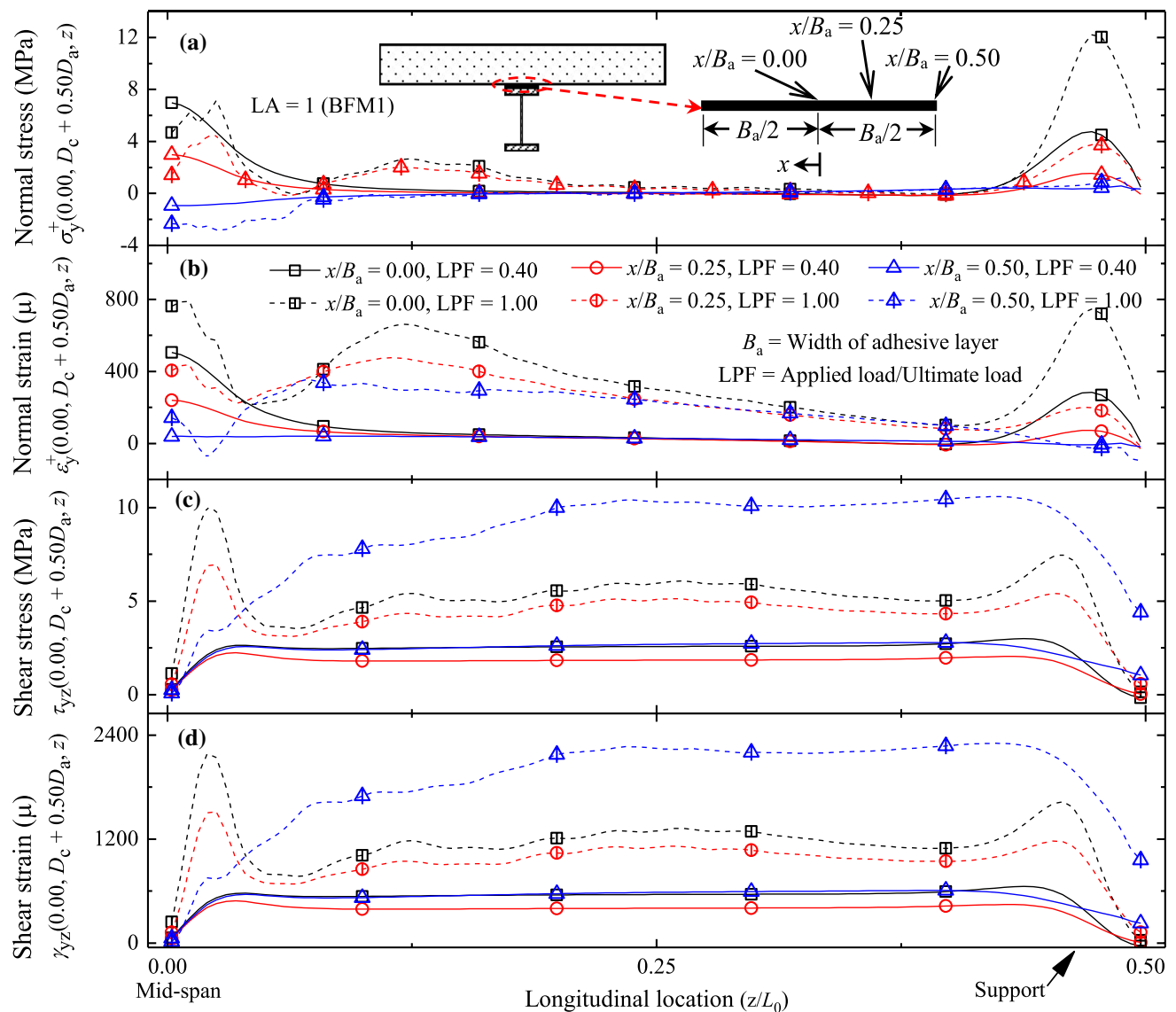


Fig. 15 Variations of considered parameters at mid-width ($x/B_a = 0.00$), quarter-width ($x/B_a = 0.25$) and outer ($x/B_a = 0.50$) longitudinal sections of the bond layer of BFM1 along the length: **a** normal stress, **b** normal strain, **c** shear stress, and **d** shear strain

stress in the quarter-width longitudinal section is found to be lower for $LPF=0.40$. At $LPF=1.00$, shear stress is highest at mid-width at mid-span. On the other hand, shear stress is highest at the outer longitudinal section far from mid-span at $LPF=1.00$.

4 Conclusions

This study presents a 3D FE model to predict the behavior of bonded steel–concrete composite flexural members (BFM) up to failure load. The developed model is validated against experimental results available in the literature. A numerical investigation is then conducted to study the behavior of the bond layer using the developed FE model. The effects of load proportion factor (LPF), loading arrangement, concrete slab width, concrete slab thickness, and Young's modulus of adhesive are investigated. Variation of normal stress, normal strain, shear stress, and shear strain in the bond layer is also studied.

It is observed that at LPF greater than 0.80, sharp peaks in shear stress, shear strain, and normal strain develop in the bond layer at the location of the imposed patch load and support in BFMs with high Young's modulus of adhesive. In case of uniformly distributed line load, normal stress developed at the support level at failure load is 3.92 times compared to mid-span loading. Among the considered cases, BFM with uniformly distributed line load experienced about four times maximum normal stress compared to BFM with mid-span loading. This happened due to the bond layer being sandwiched between high load and high support reaction at the same location.

Maximum shear stress in the bond layer is found beneath the applied load and at supports at failure load. Full shear flow and shear stress develop at a small distance from load in the bond layer in BFM when the load is applied at locations transversely away from the bond layer. Smaller width and higher depth of concrete slab lead to a smooth variation of shear stress and shear strain profile at failure load except at supports. The variation profile of shear stress at small LPFs such as 0.40 is similar to the variation profile of shear force along the length for high Young's modulus of adhesive ($E_A = 12,300$ MPa, 1230 MPa), indicating a high degree of interaction. Therefore, a high degree of interaction can be achieved using an adhesive with a high Young's modulus. Normal stress and normal strain are highest in the mid-width longitudinal section of the bond layer. Normal stress and normal strain decrease with increase in distance of adhesive fiber from mid-width of the bond layer. In some cases, normal tensile stress and normal tensile strain may appear in the outermost longitudinal section at failure load, which is small compared to the tensile capacity of adhesive. Shear stress and shear strain are higher at mid-width and the

outer longitudinal section compared to those at the quarter-width longitudinal section. The most significant parameters to affect the bond layer are identified as load proportion factor, longitudinal distribution of load, and Young's modulus of adhesive.

Research on BFMs is in preliminary stage. In order to adopt BFMs in practice, it is important to carry out investigations on various aspects. Obtaining high ductility is one of the critical aspects. Behavior of BFMs under fatigue load and seismic load has to be well understood. Also, the effect of temperature on behavior of BFM should be understood in detail before adopting these structures in practice.

Acknowledgements The authors gratefully acknowledge the financial aid from the Department of Science & Technology (DST) India for the research project titled, "Experimental and analytical studies for the short and long-term behavior of epoxy bonded steel–concrete composite bridges" (DST/TSG/STS/2011/92-G/1).

References

- Abaqus Analysis user's manual 6.13 (2013), Dassault Systems Simulia Corp., Providence, RI, USA.
- ACI 318–19. . (2019). *Building code requirements for structural concrete*. Farmington Hill: American Concrete Institute.
- Alachek, I., & Jurkiewicz, B. (2020). Experimental and finite element analysis of push-out shear test for adhesive joints between pultruded GFRP and concrete. *International Journal of Adhesion and Adhesives*, 98, 1–13.
- Amadio, C., Fedrigo, C., Fragiaco, M., & Macorini, L. (2004). Experimental evaluation of effective width in steel–concrete composite beams. *Journal of Constructional Steel Research*, 60(2), 199–220.
- Balasubramanian, R., & Rajaram, B. (2016). Study on behaviour of angle shear connector in steel–concrete composite structures. *International Journal of Steel Structures*, 16(3), 807–811.
- Bouazaoui, L., Jurkiewicz, B., Delmas, Y., & Li, A. (2008). Static behaviour of a full-scale steel–concrete beam with epoxy-bonding connection. *Engineering Structures*, 30(7), 1981–1990.
- Bouazaoui, L., Perrenot, G., Delmas, Y., & Li, A. (2007). Experimental study of bonded steel concrete composite structures. *Journal of Constructional Steel Research*, 63(9), 1268–1278.
- Carreira, D. J., & Chu, K.-H. (1985). Stress–strain relationship for plain concrete in compression. *ACI Journal*, 82(6), 797–804.
- Chaudhary, S., Pendharkar, U., & Nagpal, A. K. (2008). Service load behavior of low rise composite frames considering creep, shrinkage and cracking. *Latin American Journal of Solids and Structures*, 5(4), 237–258.
- Chiang, M. Y. M., & Herzl, C. (1994). Plastic deformation analysis of cracked adhesive bonds loaded in shear. *International Journal of Solids and Structures*, 31(18), 2477–2490.
- Da Silva, L. F. M., & Adams, R. D. (2005). Measurement of the mechanical properties of structural adhesives in tension and shear over a wide range of temperatures. *Journal of Adhesion Science and Technology*, 19(2), 109–141.
- Dai, J. G., Gao, W. Y., & Teng, J. G. (2013). Bond-slip model for FRP laminates externally bonded to concrete at elevated temperature. *Journal of Composites for Construction*, 17(2), 217–228.
- Dai, J.-G., Yokota, H., Iwanami, M., & Kato, E. (2010). Experimental investigation of the influence of moisture on the bond

- behavior of FRP to concrete interfaces. *Journal of Composites for Construction*, 14(6), 834–844.
- Do, J.-Y., & Kim, D.-K. (2013). Effect of substrate surface water on adhesive properties of high flowable VA/VeoVa-modified cement mortar for concrete patching material. *Journal of the Korea Institute for Structural Maintenance and Inspection, Korea Institute for Structural Maintenance Inspection*, 17(5), 94–104.
- Do, J. Y., & Kim, D. K. (2013). Adhesive properties of high flowable SBR-modified mortar for concrete patching material dependent on surface water ratio of concrete substrate. *Journal of the Korea Institute for Structural Maintenance and Inspection, Korea Institute for Structural Maintenance Inspection*, 17(2), 124–134.
- Drucker, D. C., & Prager, W. (1952). Soil mechanics and plastic analysis for limit design. *Quarterly of Applied Mathematics*, 10(2), 157–165.
- Gao, W. Y., Teng, J. G., & Dai, J.-G. (2012). Effect of temperature variation on the full-range behavior of FRP-to-concrete bonded joints. *Journal of Composites for Construction*, 16(16), 671–683.
- Gara, F., Ranzì, G., & Leoni, G. (2010). Short- and long-term analytical solutions for composite beams with partial interaction and shear-lag effects. *International Journal of Steel Structures*, 10(4), 359–372.
- Gupta, R. K., Kumar, S., Patel, K. A., Chaudhary, S., & Nagpal, A. K. (2015). Rapid prediction of deflections in multi-span continuous composite bridges using neural networks. *International Journal of Steel Structures*, 15(4), 893–909.
- Han, X., Akhmet, G., Hu, P., Hou, W., Baubekov, Y., & Akhmetov, M. (2020). Numerical prediction on the mechanical degradation of adhesively bonded corrugated sandwich beam after hygrothermal ageing. *Composite Structures*, 241, 112131.
- Jurkiewicz, B., Meaud, C., & Ferrier, E. (2014). Nonlinear models for steel-concrete epoxy-bonded beams. *Journal of Constructional Steel Research*, 100, 108–121.
- Jurkiewicz, B., Meaud, C., & Michel, L. (2011). Non linear behaviour of steel-concrete epoxy bonded composite beams. *Journal of Constructional Steel Research*, 67(3), 389–397.
- Kim, Y. H., Cho, H., Lee, S., & Yoon, S. J. (2011). Experimental and analytical investigations on the hat shaped shear connector in the steel-concrete composite flexural member. *International Journal of Steel Structures*, 11(1), 99–107.
- Kumar, P., & Chaudhary, S. (2019). Effect of reinforcement detailing on performance of composite connections with headed studs. *Engineering Structures*, 179, 476–492.
- Kumar, P., Patnaik, A., & Chaudhary, S. (2017). A review on application of structural adhesives in concrete and steel-concrete composite and factors influencing the performance of composite connections. *International Journal of Adhesion and Adhesives*, 77, 1–14.
- Kumar, P., Patnaik, A., & Chaudhary, S. (2018). Effect of bond layer thickness on behaviour of steel-concrete composite connections. *Engineering Structures*, 177, 268–282.
- Lebet, J.-P., & Ducret, J. (1998). Experimental and theoretical study of the behaviour of composite bridges during construction. *Journal of Constructional Steel Research*, 46(1–3), 69–70.
- Lee, J., & Fenves, G. L. (1998). Plastic-damage model for cyclic loading of concrete structures. *Journal of Engineering Mechanics*, 124(8), 892–900.
- Lublinter, J., Oliver, J., Oller, S., & Oñate, E. (1989). A plastic-damage model for concrete. *International Journal of Solids and Structures*, 25(3), 299–326.
- Luo, Y., Li, A., & Kang, Z. (2011). Reliability-based design optimization of adhesive bonded steel-concrete composite beams with probabilistic and non-probabilistic uncertainties. *Engineering Structures*, 33(7), 2110–2119.
- Luo, Y., Li, A., & Kang, Z. (2012). Parametric study of bonded steel-concrete composite beams by using finite element analysis. *Engineering Structures*, 34, 40–51.
- Matsagar, V. A. (2016). Comparative performance of composite sandwich panels and non-composite panels under blast loading. *Materials and Structures/Materiaux et Constructions*, 49(1–2), 611–629.
- Mazoz, A., Benanane, A., & Titoum, M. (2014). Push-out tests on a new shear connector of I-shape. *International Journal of Steel Structures*, 13(3), 519–528.
- Meaud, C., Jurkiewicz, B., & Ferrier, E. (2011). Investigation of creep effects in strengthened RC structures through double lap shear testing. *Composites Part B: Engineering*, 42(3), 359–366.
- Meaud, C., Jurkiewicz, B., & Ferrier, E. (2014). Steel-concrete bonding connection: An experimental study and nonlinear finite element analysis. *International Journal of Adhesion and Adhesives*, 54, 131–142.
- Naghavi, M., Rahnavard, R., Thomas, R. J., & Malekinejad, M. (2019). Numerical evaluation of the hysteretic behavior of concentrically braced frames and buckling restrained brace frame systems. *Journal of Building Engineering*, 22, 415–428.
- Nie, J.-G., Tian, C. Y., & Cai, C. S. (2008). Effective width of steel-concrete composite beam at ultimate strength state. *Engineering Structures*, 30(5), 1396–1407.
- Oehlers, D. J., & Bradford, M. A. (1995). *Composite steel and concrete structural members: Fundamental behavior*. Oxford: Pergamon Press.
- Pendharkar, U., Chaudhary, S., & Nagpal, A. K. (2011). Prediction of moments in composite frames considering cracking and time effects using neural network models. *Structural Engineering and Mechanics*, 39(2), 267–285.
- Pendharkar, U., Patel, K. A., Chaudhary, S., & Nagpal, A. K. (2015). Rapid prediction of long-term deflections in composite frames. *Steel and Composite Structures*, 18(3), 547–563.
- Pendharkar, U., Patel, K. A., Chaudhary, S., & Nagpal, A. K. (2017). Closed-form expressions for long-term deflections in high-rise composite frames. *International Journal of Steel Structures*, 17(1), 31–42.
- Rahnavard, R., Hassanipour, A., & Mounesi, A. (2016). Numerical study on important parameters of composite steel-concrete shear walls. *Journal of Constructional Steel Research*, 121, 441–456.
- Rahnavard, R., Hassanipour, A., Suleiman, M., & Mokhtari, A. (2017). Evaluation on eccentrically braced frame with single and double shear panels. *Journal of Building Engineering*, 10, 13–25.
- Rahnavard, R., Naghavi, M., Aboudi, M., & Suleiman, M. (2018). Investigating modeling approaches of buckling-restrained braces under cyclic loads. *Case Studies in Construction Materials*, 8, 476–488.
- Ramnavas, M. P., Patel, K. A., Chaudhary, S., & Nagpal, A. K. (2015). Cracked span length beam element for service load analysis of steel concrete composite bridges. *Computers and Structures*, 157, 201–208.
- Ramnavas, M. P., Patel, K. A., Chaudhary, S., & Nagpal, A. K. (2017a). Service load analysis of composite frames using cracked span length frame element. *Engineering Structures*, 132, 733–744.
- Ramnavas, M. P., Patel, K. A., Chaudhary, S., & Nagpal, A. K. (2017b). Explicit expressions for inelastic design quantities in composite frames considering effects of nearby columns and floors. *Structural Engineering and Mechanics, Techno-Press*, 64(4), 437–447.
- Riks, E. (1979). An incremental approach to the solution of snapping and buckling problems. *International Journal of Solids and Structures*, 15(7), 529–551.
- Si Larbi, A., Ferrier, E., Jurkiewicz, B., & Hamelin, P. (2007). Static behaviour of steel concrete beam connected by bonding. *Engineering Structures*, 29(6), 1034–1042.

- Souici, A., Berthet, J. F., Li, A., & Rahal, N. (2013). Behaviour of both mechanically connected and bonded steel-concrete composite beams. *Engineering Structures*, *49*, 11–23.
- Souici, A., Tehami, M., Rahal, N., Bekkouche, M. S., & Berthet, J. F. (2015). Creep effect on composite beam with perfect steel-concrete connection. *International Journal of Steel Structures*, *15*(2), 433–445.
- Su, Q. T., Yang, G. T., & Li, C. X. (2014). Structural behaviour of perforated shear connectors with flange heads in composite girders: An experimental approach. *International Journal of Steel Structures*, *14*(1), 151–164.
- Tadesse, Z., Patel, K. A., Chaudhary, S., & Nagpal, A. K. (2012). Neural networks for prediction of deflection in composite bridges. *Journal of Constructional Steel Research*, *68*(1), 138–149.
- Timoshenko, S. P., & Goodier, J. (2010). *Theory of elasticity*. McGraw Hill Education (India) Private Ltd., New Delhi.
- Varshney, L. K., Patel, K. A., Chaudhary, S., & Nagpal, A. K. (2013). Control of time-dependent effects in steel-concrete composite frames. *International Journal of Steel Structures*, *13*(4), 589–606.
- Varshney, L. K., Patel, K. A., Chaudhary, S., & Nagpal, A. K. (2019). An efficient and novel strategy for control of cracking, creep and shrinkage effects in steel-concrete composite beams. *Structural Engineering and Mechanics*, *70*(6), 751–763.
- Wang, W., Dai, J.-G., & Harries, K. A. (2013). Intermediate crack-induced debonding in RC beams externally strengthened with prestressed FRP laminates. *Journal of Reinforced Plastics and Composites*, *32*(23), 1842–1857.
- Wang, Y. H., & Nie, J.-G. (2015). Effective flange width of steel-concrete composite beam with partial openings in concrete slab. *Materials and Structures/Materiaux et Constructions*, *48*(10), 3331–3342.
- Zhan, Y., Ma, Z. J., Zhao, R., Li, G., & Xiang, T. (2016). Interface behavior between steel and concrete connected by bonding. *Journal of Bridge Engineering*, *21*(6), 04016026.
- Zhao, G., & Li, A. (2008). Numerical study of a bonded steel and concrete composite beam. *Computers and Structures*, *86*, 1830–1838.
- Zheng, H., Chen, Z., & Xu, J. (2016). Bond behavior of H-shaped steel embedded in recycled aggregate concrete under push-out loads. *International Journal of Steel Structures*, *16*(2), 347–360.
- Zheng, T., Lu, Y., & Usmani, A. (2014). Analytical model for the composite effect of coupled beams with discrete shear connectors. *Structural Engineering and Mechanics*, *52*(2), 369–389.

Publisher's Note Springer Nature remains neutral with regard to jurisdictional claims in published maps and institutional affiliations.